INTERNATIONAL JOURNAL OF HYDROGEN ENERGY 47 (2022) 33058–33066

Available online at www.sciencedirect.com

ScienceDirect

journal homepage: www.elsevier.com/locate/he

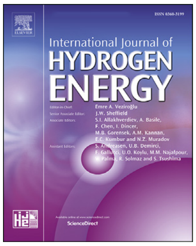

Effect of angstrom-level oxide overcoat on Sr segregation behavior of LSM electrodes

Haoyu Li [a], Hung-Sen Kang [a], Ziqi Liu [a], Orbel Barkhordarian [a], Suhan Lee [b], Yongjin Yoon [b], Min Hwan Lee [a,]*

[a] *Department of Mechanical Engineering, University of California, Merced, CA, 95343, United States*

[b] *Department of Mechanical Engineering, College of Engineering, Korea Advanced Institute of Science and Technology, South Korea*

HIGHLIGHTS

- Angstrom-level overcoat clearly tunes Sr segregation behavior in perovskites.
- A mechanistic interpretation of the overcoat effect on segregation is provided.
- Oxide overcoats with multivalent cations are effective in deterring Sr segregation.
- Chemical potential gradient of oxygen vacancies is suggested to drive Sr movement.

ARTICLE INFO

Article history:
Received 29 May 2022
Received in revised form
19 July 2022
Accepted 23 July 2022
Available online 26 August 2022

Keywords:
Solid oxide fuel cell
Sr segregation
LSM
Atomic layer deposition
Surface treatment

ABSTRACT

Long-term durability of perovskite (ABO_3)-based cathodes in solid oxide fuel cells has been largely limited by surface segregation of A-site dopant and thermal agglomeration. Since a deposition of an atomically thin oxide has proven to be highly effective in suppressing electrode agglomeration, a successful suppression of dopant segregation with the same approach will enhance the durability of cathodes significantly by killing two birds with one stone. In this report, we demonstrate that an atomic-scale overcoat with a nominal thickness of 2–3 Å is indeed an effective approach of tuning Sr segregation behavior in $La_{0.8}Sr_{0.2}MnO_3$ (LSM) if a proper choice of the overcoat material is made. Coating of a binary oxide with multi-valent cations (CeO_2 and TiO_2) desegregates Sr species into the lattice of LSM while an overcoat with single valent cations (ZrO_2 and Y_2O_3) exhibits little effect on Sr segregation. A mechanistic interpretation of the behavior is also presented based upon a series of X-ray photoelectron spectroscopy and electrochemical analyses.

Introduction

Solid oxide fuel cells (SOFCs) have an excellent potential to become widely deployed as one of the most efficient electrochemical energy conversion schemes [1]. Intensive research activities have been performed to advance the technology, but the lack of long-term durability is currently the main technological bottleneck for a wider commercial adoption [2,3]. Since the performance of a SOFC is largely limited by the reaction at the cathode, much research efforts have

---

* *Corresponding author.*
E-mail address: mlee49@ucmerced.edu (M.H. Lee).

https://doi.org/10.1016/j.ijhydene.2022.07.200

been made to improve the activity and stability of cathodes [4,5].

The majority of SOFC cathodes are in a perovskite structure (chemical formula: ABO_3) [6,7]. Most of perovskite-based conventional cathodes have either rare or alkaline earths doped in the A-site for ionic and electronic conductivity while 3d, 4d or 5d transition metals with flexible valence states occupy the B-site for catalytic activity [8,9]. Upon sintering perovskite-based oxides in an oxidizing environment, A-site dopants (most notably, Sr) tend to segregate to the surface due to their larger size compared to the host cation (La^{3+}) and subsequently form insulating phases on the surface or rearrange the surface structure [10–13]. This eventually degrades surface oxygen exchange kinetics and electrochemical performance. The dopant segregation, besides microstructural sintering and surface poisoning, has been regarded as the major factor of electrode performance decay [5,14–16].

There are various theories regarding the driving force of dopant segregation, elastic and electrostatic interactions have been widely accepted as the major mechanisms [8,17]. First, elastic energy is incurred largely by the size mismatch between the host and dopant cations at the A-site; Sr^{2+} dopant is larger than La^{3+} host by ~5.9% [18]. On the other hand, the electrostatic interaction-based Sr segregation is ascribed to the positively charged oxygen vacancies ($V_O^{\cdot\cdot}$) in the Kröger-Vink notation) heavily accumulated on the surface [19–22]. Oxygen vacancies are readily formed on the surface because of lower cationic coordination numbers compared to those in the bulk [8]. The surface oxygen vacancies attract negatively charged Sr (Sr'_A in the Kröger-Vink notation) toward the surface and facilitates Sr segregation. Tsvetkov et al. demonstrated that if cations of low reducibility were coated on the surface of $La_{0.8}Sr_{0.2}CoO_3$ (LSC), the surface $V_O^{\cdot\cdot}$ concentration decreases leading to a suppression of Sr surface segregation [19]. More recently, Choi et al. showed that an overcoat of few nanometer-thick $Gd_{0.1}Ce_{0.9}O_{2-\delta}$ (GDC) on the surface of $Sm_{0.5}Sr_{0.5}CoO_{3-\delta}$ (SSC) reduces the oxygen vacancy concentration on the SSC surface and suppresses surface segregation of Sr'_A, affording an excellent electrode durability [23]. More recently, Zhuang et al. reported that the surface stoichiometry of $(La_{0.6}Sr_{0.4})_{0.95}Co_{0.2}Fe_{0.8}O_{3-\delta}$ (LSCF) through an atom trapping scheme can form Sr and O vacancies and enhance the oxygen redox activity and durability [24].

In this report, we present a behavior seemingly contradicting to the aforementioned mechanism of electrostatic force-driven Sr segregation; a higher concentration of oxygen vacancies on the surface of LSM tends to suppress Sr segregation toward surface or even incorporate Sr species back into the lattice of LSM. A different mechanism – diffusion of oxygen vacancies driven by vacancy concentration gradient – is proposed based upon a series of X-ray photoelectron spectroscopy observations. To induce a change in the oxygen vacancy concentration on LSM surface, four different metal oxides of angstrom-level thicknesses are coated by the atomic layer deposition (ALD). ALD affords a precise control of uniformity and thickness at a sub-nanometer level. By utilizing the layer-by-layer deposition, the thickness of a film can be tailored by the number of ALD cycles [15]. The sequential and self-limiting characteristics of ALD enables an unprecedented control over the thickness and uniformity even on a substrate with highly corrugated geometry like those of a porous electrode.

Experimental

Cell preparations

The LSM powder was synthesized by using the glycine-nitrate combustion method. $La(NO_3)_3\cdot6H_2O$, $Sr(NO_3)_2$, and $Mn(NO_3)_2\cdot4H_2O$ with a molar ratio of 0.8:0.2:1 were dissolved in a minimal amount of deionized water while being stirred on a hot plate. Glycine was used as the reducing agent. The molar ratio between the sum of the nitrates and glycine was 1:1. Combustion was performed after the mixture was dehydrated in air. The resulting powder was sintered at 850 °C for 3 h in a zirconia container to obtain LSM. The crystallography of LSM powder was confirmed by X-ray diffraction (XRD).

The cells used for electrochemical impedance spectroscopy (EIS) testing are in a symmetric configuration. On a commercial YSZ substrate (thickness: 250–300 μm; diameter: 20 mm; Fuelcellmaterials.com), a 10 μm thick $Ga_{0.2}Ce_{0.8}O_2$ (GDC) interlayer was screen printed on both sides of the YSZ. Onto each GDC layer, a layer of LSM (namely, functional layer) was deposited again by screen-printing, followed by a sintering at 850 °C for 3 h. We limited the sintering temperature at 850 °C to avoid an excessive Sr segregation in the as-prepared LSM layers. An atomic layer deposition (ALD) was performed onto each side of the functional layers to deposit metal oxides of ~2–3 Å in nominal thickness; 8 cycles of TiO_2, 10 cycles of CeO_2, 3 cycles of ZrO_2 and 3 cycles of Y_2O_3 (namely, LSM-Ti, LSM-Ce, LSM-Zr, and LSM-Y, respectively). Finally, two more layers of LSM were screen-printed and sintered at 850 °C for 3 h to use them as the current collecting layer. The GDC interlayer is placed to prevent any unexpected reactions between YSZ and LSM layers. The slurries for GDC and LSM were made by mixing GDC nano-powder or LSM power with ethyl cellulose, Hypermer KD-1, and terpineol in an appropriate ratio. A circular reaction area of 0.35 cm^2 was formed in all symmetric cells.

The ALD was performed in a commercial ALD system (ICOT Inc). $Zr(NMe_2)_4$, $Y(MeCp)_3$, $Ce(iPrCp)_3$, and $Ti(NMe_2)_4$ were used as the precursors of Zr, Y, Ce, and Ti respectively. Nitrogen (99.9%) and deionized water were used as the purging gas and oxygen source, respectively. The chamber temperature was set at 250 °C, and the canister temperatures for Zr, Y, Ce, and Ti precursors were 80, 150, 150, and 80 °C, respectively. Purging gas was fed at a constant flow rate of 3 sccm.

Physical characterization

A field-emission scanning electron microscopy (FE-SEM, Zeiss Gemini 500) was used at 3 kV to observe the microstructure. X-ray photoelectron spectroscopy (XPS) was performed on a Nexus system (Thermo Fisher Scientific) using monochromated, micro-focused, low power Al Kα X-ray source for excitation and a 180°, double-focusing, hemispherical analyzer with 128-channel detector (10–400 μm spot size with adjustable sample holder incident to X-ray beam from 0° to 60°). The phase and composition of samples were evaluated by XRD using a PANalytical X'Pert Pro system with Co Kα radiation ($\lambda = 1.78897$ Å).

Electrochemical characterization

Electrochemical characterization was performed by electrochemical impedance spectroscopy (EIS; Bio-Logic SP-200) with 20 mV of AC perturbation at the open circuit condition. Durability tests were performed in a custom-made Cr-free SOFC test station in air to avoid possible Cr poisoning during operation. For durability test, silver mesh was used to collect current. A 5 kg load was applied through the cell to ensure a solid contact between the cell and current collecting mesh.

Results and discussion

Each of the four different metal oxides (ZrO_2, Y_2O_3, CeO_2, and TiO_2) with a similar nominal thickness (2–3 Å) was introduced by ALD on a LSM backbone. As shown in Fig. 1, the ALD treatment was performed on the first layer of porous LSM backbone (~20 μm), and we call it the functional layer (FL). Two additional LSM layers were further screen-printed on top of the FL for current collection. Due to the low ionic conductivity of LSM [25], most ORR reaction is expected to occur in a close vicinity to the electrode-electrolyte interface within the FL.

First, XRD analysis is performed to identify the crystal phase of LSM powder synthesized by the glycine nitrate combustion method. Fig. 2 shows that LSM is in a rhombohedral phase ($R\bar{3}c$ space group) without a noticeable trace of $Sr(OH)_2$ and SrO phase. There is no additional peak appearing after a prolonged exposure to 750 °C for 50 h or 250 h. ALD treated samples do not exhibit discernible peaks other than those found in the bare LSM either, which is likely because the amount of ALD-derived oxide is negligible compared to the LSM pellet [26].

To better understand the effect of angstrom-level metal oxide overcoat on the surface chemistry, XPS analysis is performed on each sample (LSM-bare and four ALD-coated LSM samples) at 3 different stages of aging at 750 °C: 0 h, 50 h, and 250 h. Sr 3d spectra are deconvoluted into two constituents as shown in Fig. 3a–c and Fig. S1: Sr_α (~132.1 eV) assigned to lattice Sr, and Sr_β (~133.7 eV) assigned to surface Sr found in Sr-containing phases such as SrO, $Sr(OH)_2$ and $SrCO_3$ [19]. Once Sr species reach the surface by segregation, they subsequently react with surrounding gas and form compounds such as hydroxides and carbonates [20]. Unlike the other samples, those with TiO_2 and CeO_2 overcoat (i.e., LSM-Ti and LSM-Ce) show a significant decrease in the surface Sr content after 250 h, as shown in Fig. 3d. The fraction of surface Sr quantified by $[Sr_\beta]/([Sr_\alpha]+[Sr_\beta])$ in LSM-Ti decreased from 37.5% to 17.8% for 250 h, and the fraction in LSM-Ce decreased from 37.0% to 16.0% during the same time.

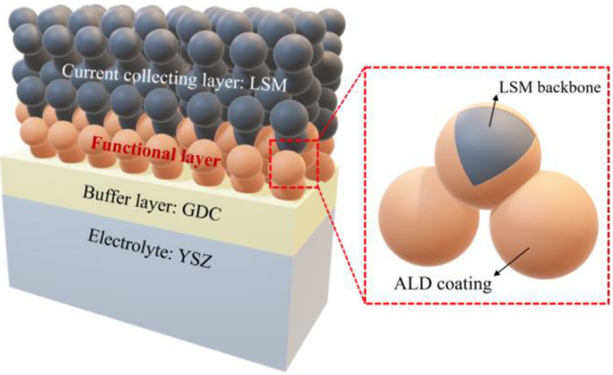

Fig. 1 – A schematic diagram of the cell configuration, showing half of a symmetric cell.

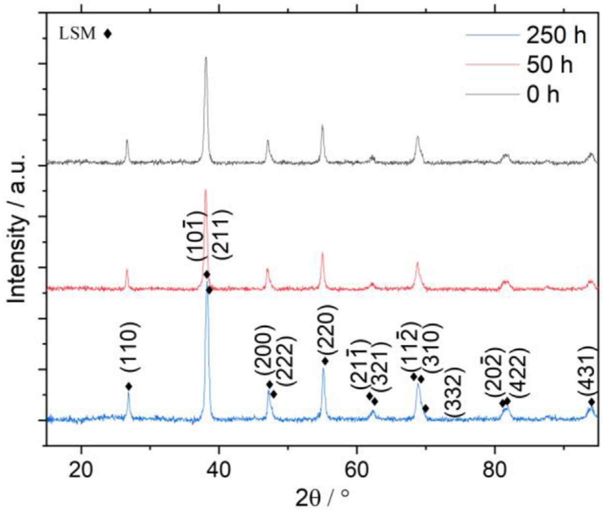

Fig. 2 – XRD spectra of LSM-bare after exposing it to air at 750 °C for 0 h, 50 h and 250 h.

As an alternative method of gauging the degree of segregation, an angle resolved XPS (ARXPS) was also performed. By varying the angle at which the emitted electrons are detected with respect to the sample direction, one can obtain spectra relevant to different depths of the sample. While the usual XPS probes a depth of ~10 nm, a shallower depth is probed by detecting emitted electrons at a tilted angle [27]. In our system, the ratio of the signal intensity obtained at the collection angle of 60° to those of 0° is ~0.29 for an LSM-bare sample, indicating that the detection depth for sample with 60° emission angle is approximated ~2.9 nm. Here, the collection angle means the angle formed between the direction of incident beam and the direction normal to the sample surface. Although the samples are porous and corrugated, as opposed to uniform and dense, the ARXPS characterization is expected to provide at least a qualitative sense of how the chemical states in the very vicinity of the surface are different from those within the lattice considering the size of each particle-like feature is >~50 nm, significantly larger than the detection depth. A normalized parameter, Sr^* is defined as follows to indicate the degree of Sr segregation toward surface.

$$Sr^* = \frac{[Sr_{60^\circ}]/([Sr_{60^\circ}] + [La_{60^\circ}])}{[Sr_{0^\circ}]/([Sr_{0^\circ}] + [La_{0^\circ}])} \tag{1}$$

where [Sr] and [La] are the atomic concentrations of Sr and La, respectively, obtained from the spectra at their corresponding

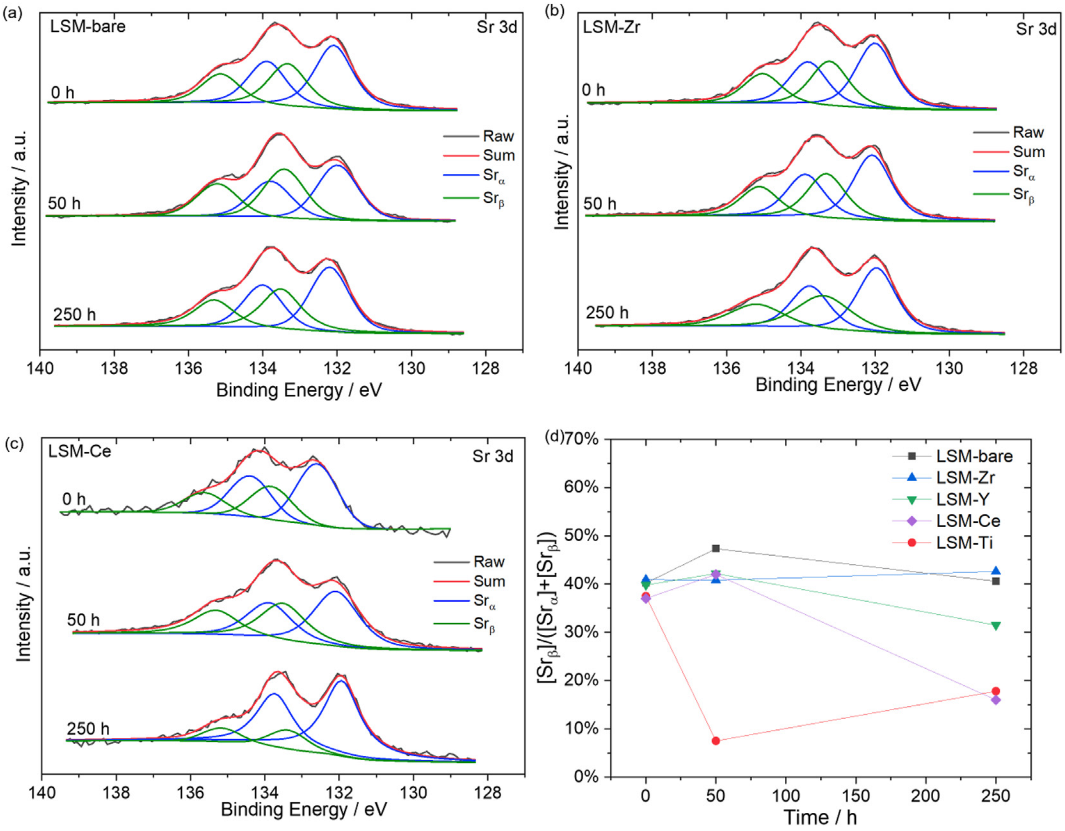

Fig. 3 – (a–c) Sr 3d spectra of (a) LSM-bare, (b) LSM-Zr, and (c) LSM-Ce after exposing them to air at 750 °C for 0, 50, and 250 h. The spectra are deconvoluted into two parts: surface Sr (green) and lattice Sr (blue). Sr 3d spectra of LSM-Y and LSM-Ti are presented in Fig. S1. (d) Relative concentrations of surface Sr as a function of thermal exposure time. All data are obtained at the collection angle of 0°. (For interpretation of the references to colour in this figure legend, the reader is referred to the Web version of this article.)

collection angles. As shown in Fig. 4, all the samples exhibit an initial Sr^* value of 1 ± 0.05, indicating a uniform depth-wise distribution of Sr species in the as-prepared samples. While LSM-bare and LSM-Zr exhibit a slight increase of Sr^* after 250 h at 750 °C, LSM-Ti and LSM-Ce show a significant decrease in Sr^*, reflecting a desegregation behavior (meaning Sr movement from the surface to the bulk) during the heat exposure. This is well aligned with the data in Fig. 3 that showed a decreased amount of surface Sr species in both LSM-Ti and LSM-Ce. The similarity in the time evolution of Sr species as observed from the two separate approaches – peak deconvolution (Fig. 3) and ARXPS analysis (Fig. 4) – convincingly suggest that an atomic scale overcoat by TiO_2 and CeO_2 is highly effective in desegregating Sr species from surface into the bulk. On the other hand, the samples coated with Y_2O_3 and ZrO_2 (i.e., LSM-Y and LSM-Zr) show relatively minor difference from LSM-bare in the segregation behavior.

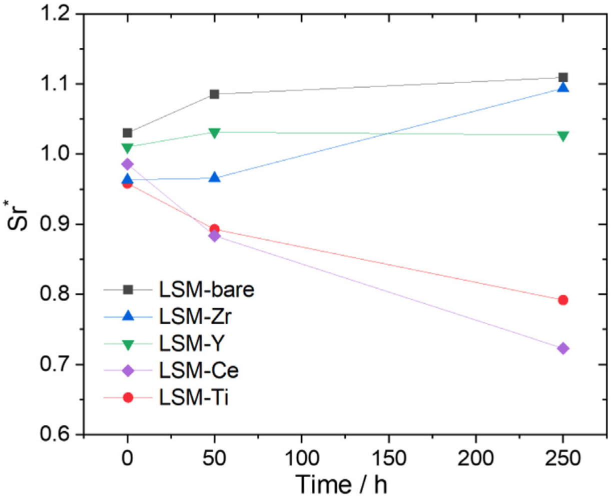

Fig. 4 – Degree of Sr segregation based on the total amount of Sr in XPS data, normalized by the total amount of A-site species in the same condition.

Looking at the results presented above, we recognize that samples coated with an oxide of multi-valent cations (i.e., LSM-Ce and LSM-Ti; namely, OMC) show a continuous desegregation behavior whereas those coated with an oxide of single valent cations (i.e., LSM-Zr and LSM-Y; OSC) show a minor Sr segregation. To better understand the correlation between the cationic multi-valency and segregation behavior, the evolution of O 1s peak is additionally observed as shown in Fig. 5; the spectra for LSM-bare, LSM-Zr, and LSM-Ce are presented in Fig. 5a–c, and those for LSM-Y and LSM-Ti are provided Fig. S2. The peaks at ~529.7 eV, 531.2 eV and 532.2 eV are ascribed to the lattice oxygen (named as O_α), oxygen defect

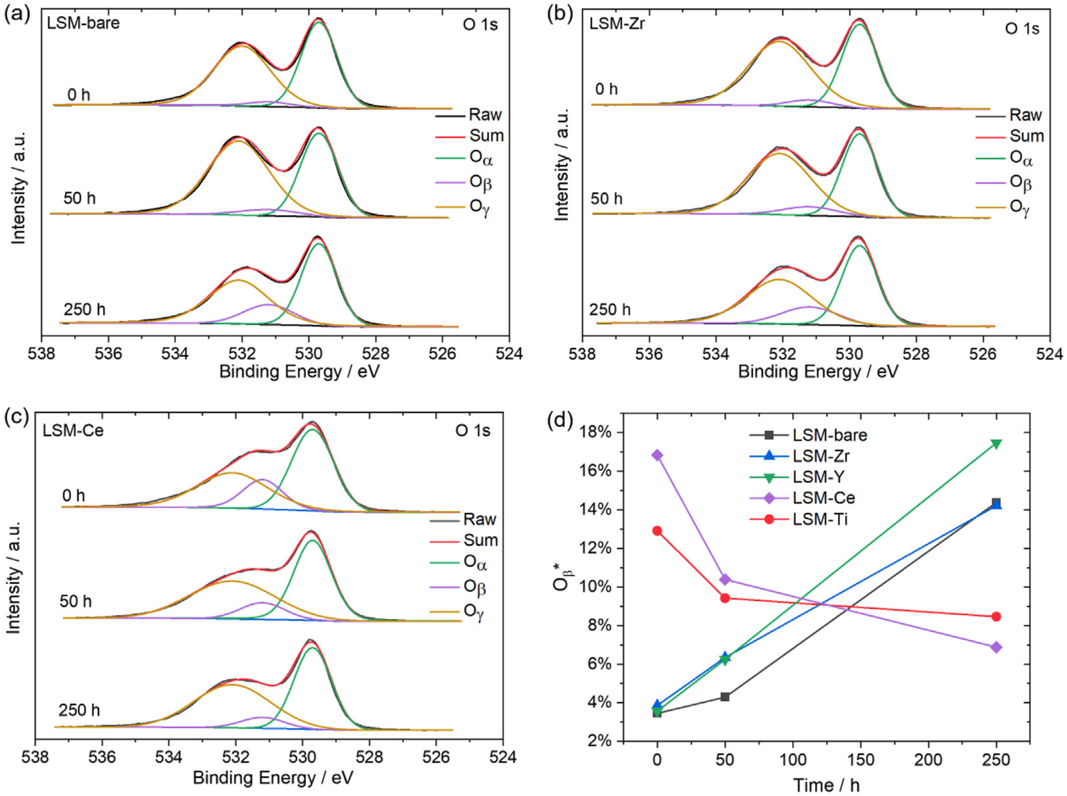

Fig. 5 – (a–c) O 1s spectra of (a) LSM-bare, (b) LSM-Zr and (c) LSM-Ce after exposing them to air at 750 °C for 0, 50, and 250 h at the electron collection angle of 0°. The spectra are deconvoluted into three parts: lattice oxygen (green), oxygen vacancy (purple) and surface oxygen (brown). O 1s spectra of LSM-Y and LSM-Ti are presented in Fig. S2. (d) Relative concentrations of oxygen vacancies quantified based upon the peak deconvolution, as a function of thermal exposure time. (For interpretation of the references to colour in this figure legend, the reader is referred to the Web version of this article.)

(i.e., oxygen vacancy; O_β) and surface adsorbed oxygen species (e.g. hydroxides; O_γ), respectively [28–31]. After fitting the spectra, the relative amount of oxygen vacancy is quantified by $[O_\beta]/([O_\alpha]+[O_\beta]+[O_\gamma])$, which is named as O_β^*. As shown in Fig. 5d, two different trends in the evolution of O_β^* are clearly visible. OMCs (i.e., LSM-Ce and LSM-Ti) start with a relatively high O_β^* but exhibit a decreasing trend while OSCs (i.e., LSM-Zr and LSM-Y) show a clear increasing trend with a low starting value. The same trend is visible from the O 1s peak observed at the collection angle of 60° (Fig. S3), which is supposed to reveal a more surface-specific information.

The high initial O_β^* values of OMCs are ascribed to the oxygen defects formed by the overcoat rather than the underlying LSM. This is partially supported by the considerable amount of trivalent Ce and Ti as detected by the Ce 3d and Ti 2p spectra (Fig. S4; Table S1). On the other hand, the inflexible valence states of Zr and Y in OSCs would incur little formation of oxygen vacancies within the overcoat. Therefore, the finite amount of initial O_β^* values of OSCs shown in Fig. 5b, albeit small, are likely to be detected from LSM lattice in the vicinity of surface, not from the overcoat layer. This is further supported by the Mn valence state around the surface of LSM (Fig. S5b). The Mn valence states of OSCs are initially in the range of 3.3–3.5 while those of OMCs are significantly higher than these values (LSM-Ce = 3.6; LSM-Ti = 4.1). Considering the charge neutrality requirement, a lower Mn valence state indicates the existence of more of oxygen vacancies in the lattice. It is noted that the Mn valence state of OMCs at collection angle of 0° (which probes a deeper depth from the surface; Fig. S5a) are lower than those measured at 60°. This indicates that oxygen vacancies in LSM are less populated in the vicinity of its surface compared to the bulk (i.e., within the lattice).

Therefore, it can be deduced that a proper ALD coating, even with an angstrom-level thickness, has distinctly affected the migration of oxygen species around the overcoat-LSM interface; the overcoat of OMCs attracts oxygen vacancies from the bulk of LSM to the interface while those of OSCs do not.

To summarize the XPS observations, OMCs show a significant desegregation of Sr species and a drastic decrease of surface oxygen vacancy concentration during their exposure to 750 °C. On the other hand, OSCs exhibit a minor change in the surface Sr content and a considerable increase of oxygen vacancy concentration during the same period. Fig. 6 depicts the conjectured movements of ionic species around the surface based upon these observations.

First, in OMCs, the initially formed oxygen vacancies within the overcoat diffuses into the bulk of LSM. Simultaneously, Sr species from the SrO layer are incorporated into the LSM lattice while La species are segregated to the surface

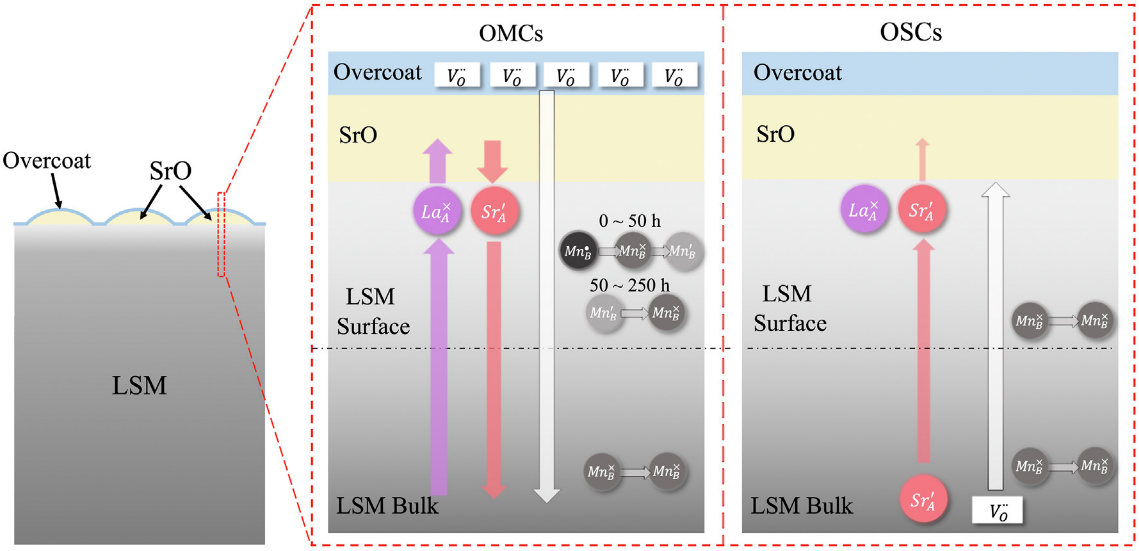

Fig. 6 – A simplified schematic drawing to present the conjectured movements of ionic species during thermal exposure at 750 °C.

as shown in Figs. S5c–d, probably forming La_2O_3. Within the LSM close to the surface, Mn species are reduced significantly for the first 50 h and subsequently oxidized for the remaining hours at a mild rate (Fig. S5b). The change in the Mn valence state evolution can be partially explained by the decelerated oxygen vacancy incorporation (Fig. 5d) after 50 h due to the limited amount of available oxygen vacancies. In the overcoat layer, the loss of oxygen vacancies is charge-balanced by the oxidation of overcoat cations (i.e., Ti or Ce ions), which is supported by XPS observations (summarized in Table S1). In the LSM surface layer, the incorporation of Sr species is charge-balanced by the introduction of oxygen vacancies from the overcoat.

On the other hand, in OSCs, the overall movement of ionic species are relatively weak compared to those observed in OMCs. There is little oxygen vacancy present in the overcoat from the start whereas they are more populated in the LSM lattice compared to OMCs. It is conjectured that both oxygen vacancies and Sr species segregate to the surface side, which will satisfy the local charge neutrality requirement in each layer. According to Fig. 3d, there is not an appreciable change in the surface Sr content, indicating the segregated Sr does not form additional Sr oxide (e.g., SrO) on the surface of OSCs.

Fig. 7 shows the time evolution of normalized polarization resistances (R_p) at 750 °C. LSM-bare shows a dramatic degradation in electrode performance by changing R_p from 1.87 to 4.90 Ω cm^2 and the characteristic frequency (f_c) from ~2000 Hz–164 Hz after 200 h. The f_c change indicates that the rate-determining step (RDS) of the electrode reaction shifted from a fast process (e.g., charge transfer reaction) to a slow process (e.g., adsorption or diffusion) [32]. Compared to the LSM-bare that degraded by a factor of 2.62, all the samples with an ALD overcoat exhibit a much more stable performance. This is mainly ascribed to the excellent efficacy of ALD overcoat in suppressing agglomeration of LSM backbone [26]. As shown in Fig. 8, the median LSM particle size of LSM-bare changed from 52.8 nm to 71.1 nm for 200 h at 750 °C; see Supplementary for details of quantifying particle size. On the other hand, all the ALD-coated samples maintained the size to be smaller than ~60 nm (LSM-Zr = 57.9 nm; LSM-Y = 60.4 nm; LSM-Ti = 50.6 nm; LSM-Ce = 51.0 nm) during the same thermal exposure. The close correlation between the particle size and electrode performance can be ascribed to the reasoning that a smaller particle size would render a larger amount of oxygen adsorption sites and triple phase boundary regions. While the evolution of R_p is mainly dictated by the LSM particle size, the R_p values after 200 h (Fig. 7a) show that OMCs afford a slightly better long-term durability than OSCs.

It is noteworthy that the LSM particle size of OMCs become even smaller after 200 h of thermal exposure (from 52.8 nm to 51.0 nm for LSM-Ce, and to 50.6 nm for LSM-Ti), which is unexpected in the context of thermally driven sintering process. We ascribe the phenomena to the incorporation of surface Sr species (such as $Sr(OH)_2$ and SrO) back into the LSM lattice. An incorporation of a mole of SrO would accompany a formation of a half mole of La_2O_3 as shown in Eqn. (2). Therefore, to explain the decrease of LSM particle sizes, it is reasonable to assume that an initial presence of A-site vacancies provided the sites for incorporating Sr species from the surface.

$$2SrO + 2La_{A(LSM)}^{\times} + O_{O(LSM)}^{\times} \rightarrow La_2O_3 + 2Sr'_{A(LSM)} + V_{O(LSM)}^{\cdot\cdot} \quad (2)$$

As revealed by Sr 3d spectra in Fig. 3, the as-prepared LSM-bare has appreciable amount of surface Sr species, and the OMCs show an explicit desegregation behavior, well aligned with the trend of LSM particle size evolution (i.e., the particles of OMCs became smaller while those for OSCs grew). However, the correlation between the evolutions of R_p and particle size is less explicit among ALD-coated samples than those between LSM-bare and ALD-coated samples. As shown in Fig. S10, all the samples show an initial drop in R_p for the first ~50 h followed by a gradual and consistent increase, and the amount of the initial R_p drop is somewhat larger in OMCs.

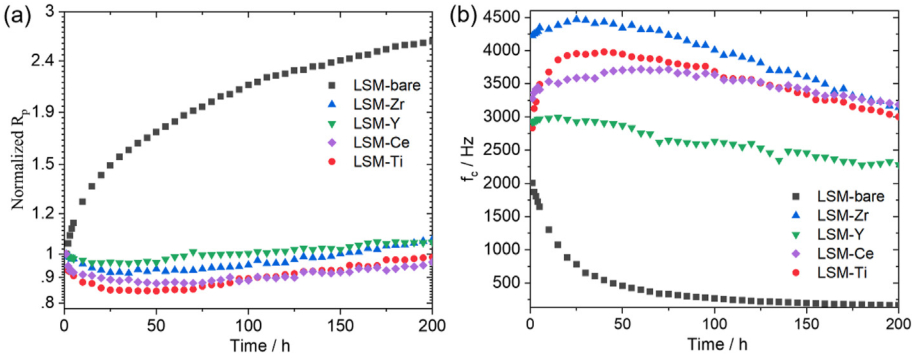

Fig. 7 – **Time evolution of normalized R_p (a) and characteristic frequency, (f_c). The normalized R_p is obtained by dividing R_p by the initial value for each sample. All the data are deduced from the EIS data shown in Fig. S6.**

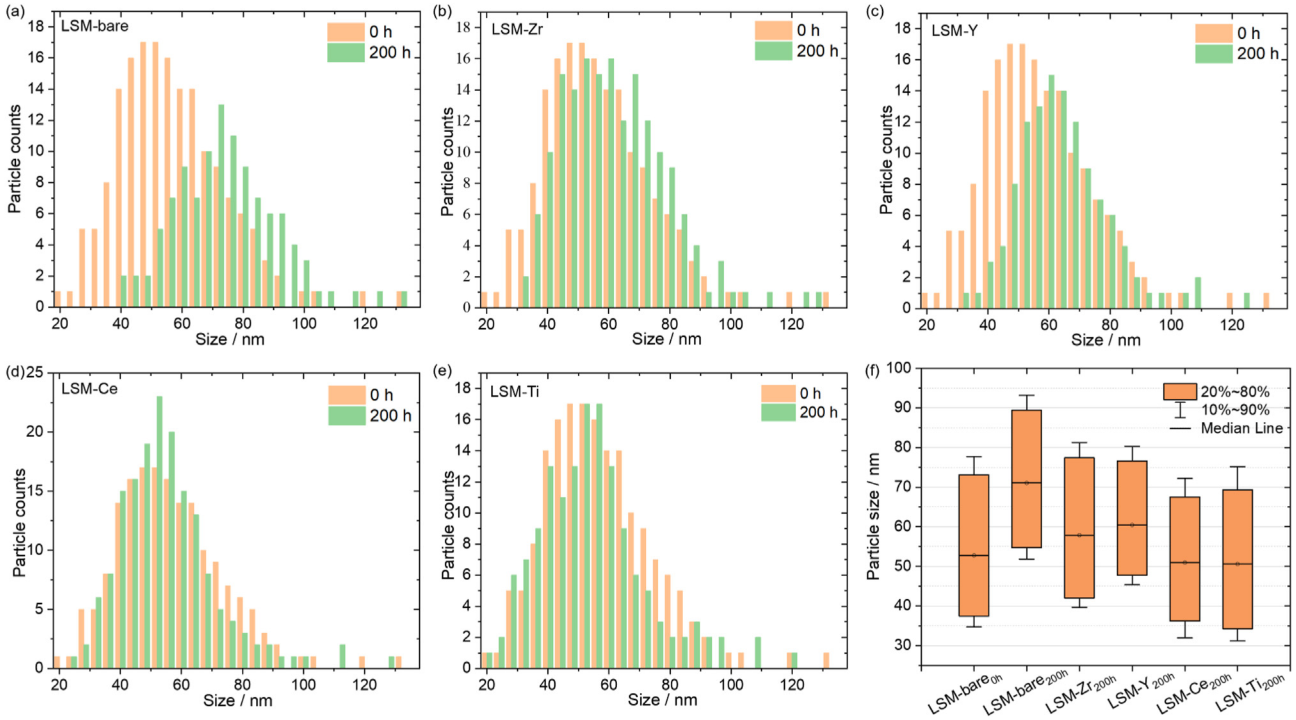

Fig. 8 – **(a–e) Size distribution of LSM particles in initial stage (0 h) and final stage (200 h) at 750 °C, and (f) the corresponding box chart of LSM particle sizes. Graphs are based upon the FE-SEM images shown in Figs. S8 and S9.**

Conclusions

In this paper, we demonstrate that even an atomic-scale overcoat with a nominal thickness of 2–3 Å can affect the Sr segregation behavior in LSM. Considering the extreme thickness of the overcoat, we believe this approach is promising in controlling the migration of ionic species and the formation/annihilation of surface oxides, which are highly related to the surface kinetics of electrode reactions. An overcoat of binary oxide with multi-valent cations (CeO_2 and TiO_2) tends to drive Sr species into the lattice of LSM while an overcoat with single valent cations (ZrO_2 and Y_2O_3) exhibits little effect on Sr segregation. This is ascribed to the initial differences in the amount of surface oxygen vacancies and resulting chemical potential gradient around the surface. A more systematic study to reveal the overcoat effect is reserved for an upcoming report, which is based upon a flat and dense electrode for a more explicit parametric study.

Declaration of competing interest

The authors declare that they have no known competing financial interests or personal relationships that could have appeared to influence the work reported in this paper.

Acknowledgements

The authors acknowledge the support from the National Science Foundation (DMR 1753383) and NASA MIRO program (Grant No. NNX15AQ01A).

Appendix A. Supplementary data

Supplementary data to this article can be found online at https://doi.org/10.1016/j.ijhydene.2022.07.200.

REFERENCES

[1] Zhao C, Li Y, Zhang W, Zheng Y, Lou X, Yu B, et al. Heterointerface engineering for enhancing the electrochemical performance of solid oxide cells. Energy Environ Sci 2020;13:53–85. https://doi.org/10.1039/C9EE02230A.

[2] Chen K, Jiang SP. Review—materials degradation of solid oxide electrolysis cells. J Electrochem Soc 2016;163:F3070–83. https://doi.org/10.1149/2.0101611jes.

[3] Mahato N, Banerjee A, Gupta A, Omar S, Balani K. Progress in material selection for solid oxide fuel cell technology: a review. Prog Mater Sci 2015;72:141–337. https://doi.org/10.1016/j.pmatsci.2015.01.001.

[4] Adler SB. Factors governing oxygen reduction in solid oxide fuel cell cathodes. Chem Rev 2004;104:4791–843. https://doi.org/10.1021/cr020724o.

[5] Jung W, Tuller HL. Investigation of surface Sr segregation in model thin film solid oxidefuel cell perovskite electrodes. Energy Environ Sci 2012;5:5370–8. https://doi.org/10.1039/C1EE02762J.

[6] Sunarso J, Hashim SS, Zhu N, Zhou W. Perovskite oxides applications in high temperature oxygen separation, solid oxide fuel cell and membrane reactor: a review. Prog Energy Combust Sci 2017;61:57–77. https://doi.org/10.1016/j.pecs.2017.03.003.

[7] Jun A, Kim J, Shin J, Kim G. Perovskite as a cathode material: a review of its role in solid-oxide fuel cell technology. Chemelectrochem 2016;3:511–30. https://doi.org/10.1002/celc.201500382.

[8] Koo B, Kim K, Kim JK, Kwon H, Han JW, Jung W. Sr segregation in perovskite oxides: why it happens and how it exists. Joule 2018;2:1476–99. https://doi.org/10.1016/j.joule.2018.07.016.

[9] Sun C, Hui R, Roller J. Cathode materials for solid oxide fuel cells: a review. J Solid State Electrochem 2009;14:1125–44. https://doi.org/10.1007/s10008-009-0932-0.

[10] Simner SP, Anderson MD, Engelhard MH, Stevenson JW. Degradation mechanisms of La-Sr-Co-Fe-O3 SOFC cathodes. Electrochem Solid State Lett 2006;9:A478. https://doi.org/10.1149/1.2266160.

[11] Baqué LC, Soldati AL, Teixeira-Neto E, Troiani HE, Schreiber A, Serquis AC. Degradation of oxygen reduction reaction kinetics in porous La0.6Sr0.4Co0.2Fe0.8O3-δ cathodes due to aging-induced changes in surface chemistry. J Power Sources 2017;337:166–72. https://doi.org/10.1016/j.jpowsour.2016.10.090.

[12] Rupp GM, Opitz AK, Nenning A, Limbeck A, Fleig J. Real-time impedance monitoring of oxygen reduction during surface modification of thin film cathodes. Nat Mater 2017;16:640–5. https://doi.org/10.1038/nmat4879.

[13] Sun Y, He S, Saunders M, Chen K, Shao Z, Jiang SP. A comparative study of surface segregation and interface of La0·6Sr0·4Co0·2Fe0·8O3-δ electrode on GDC and YSZ electrolytes of solid oxide fuel cells. Int J Hydrogen Energy 2021;46:2606–16. https://doi.org/10.1016/j.ijhydene.2020.10.113.

[14] Jiang SP, Chen X. Chromium deposition and poisoning of cathodes of solid oxide fuel cells – a review. Int J Hydrogen Energy 2014;39:505–31. https://doi.org/10.1016/j.ijhydene.2013.10.042.

[15] Karimaghaloo A, Koo J, Kang H-S, Song SA, Shim JH, Lee MH. Nanoscale surface and interface engineering of solid oxide fuel cells by atomic layer deposition. Int J Precis Eng Manuf Technol 2019;6:611–28. https://doi.org/10.1007/s40684-019-00090-9.

[16] Jiang SP. Development of lanthanum strontium cobalt ferrite perovskite electrodes of solid oxide fuel cells – a review. Int J Hydrogen Energy 2019;44:7448–93. https://doi.org/10.1016/J.IJHYDENE.2019.01.212.

[17] Irvine JTS, Neagu D, Verbraeken MC, Chatzichristodoulou C, Graves C, Mogensen MB. Evolution of the electrochemical interface in high-temperature fuel cells and electrolysers. Nat Energy 2016;1:15014. https://doi.org/10.1038/nenergy.2015.14.

[18] Shannon RD. Revised effective ionic radii and systematic studies of interatomic distances in halides and chalcogenides. Acta Crystallogr A 1976;32:751–67. https://doi.org/10.1107/S0567739476001551.

[19] Tsvetkov N, Lu Q, Sun L, Crumlin EJ, Yildiz B. Improved chemical and electrochemical stability of perovskite oxides with less reducible cations at the surface. Nat Mater 2016;15:1010–6. https://doi.org/10.1038/nmat4659.

[20] Lee W, Han JW, Chen Y, Cai Z, Yildiz B. Cation size mismatch and charge interactions drive dopant segregation at the surfaces of manganite perovskites. J Am Chem Soc 2013;135:7909–25. https://doi.org/10.1021/ja3125349.

[21] Fister TT, Fong DD, Eastman JA, Baldo PM, Highland MJ, Fuoss PH, et al. In situ characterization of strontium surface segregation in epitaxial La0.7Sr0.3MnO3 thin films as a function of oxygen partial pressure. Appl Phys Lett 2008;93:151904. https://doi.org/10.1063/1.2987731.

[22] Kuyyalil J, Newby D, Laverock J, Yu Y, Cetin D, Basu SN, et al. Vacancy assisted SrO formation on La0.8Sr0.2Co0.2Fe0.8O3−δ surfaces—a synchrotron photoemission study. Surf Sci 2015;642:33–8. https://doi.org/10.1016/j.susc.2015.08.001.

[23] Choi M, Ibrahim IAM, Kim K, Koo JY, Kim SJ, Son J-W, et al. Engineering of charged defects at perovskite oxide surfaces for exceptionally stable solid oxide fuel cell electrodes. ACS Appl Mater Interfaces 2020;12:21494–504. https://doi.org/10.1021/acsami.9b21919.

[24] Zhuang Z, Li Y, Yu R, Xia L, Yang J, Lang Z, et al. Reversely trapping atoms from a perovskite surface for high-performance and durable fuel cell cathodes. Nat Catal 2022;5:300–10. https://doi.org/10.1038/s41929-022-00764-9.

[25] Skinner SJ, Kilner JA. Oxygen ion conductors. Mater Today 2003;6:30–7. https://doi.org/10.1016/S1369-7021(03)00332-8.

[26] Li H, Kang H-S, Grewal S, Nelson AJ, Song SA, Lee MH. How an angstrom-thick oxide overcoat enhances durability and activity of nanoparticle-decorated cathodes in solid oxide fuel cells. J Mater Chem 2020;8:15927–35. https://doi.org/10.1039/D0TA02915G.

[27] Sha Z, Cali E, Kerherve G, Skinner SJ. Oxygen diffusion behaviour of A-site deficient (La0.8Sr0.2)0.95Cr0.5Fe0.5O3−δ perovskites in humid conditions. J Mater Chem 2020;8:21273–88. https://doi.org/10.1039/D0TA08899D.

[28] Li X, Ma J, Yang L, He G, Zhang C, Zhang R, et al. Oxygen vacancies induced by transition metal doping in γ-MnO2 for highly efficient ozone decomposition. Environ Sci Technol 2018;52:12685–96. https://doi.org/10.1021/ACS.EST.8B04294.

[29] Jia J, Zhang P, Chen L. Catalytic decomposition of gaseous ozone over manganese dioxides with different crystal structures. Appl Catal B Environ 2016;189:210–8. https://doi.org/10.1016/J.APCATB.2016.02.055.

[30] Jain S, Shah J, Negi NS, Sharma C, Kotnala RK. Significance of interface barrier at electrode of hematite hydroelectric cell

for generating ecopower by water splitting. Int J Energy Res 2019;43:4743–55. https://doi.org/10.1002/ER.4613.

[31] Liu Z, Andrade AM, Grewal S, Nelson AJ, Thongrivong K, Kang H-S, et al. Trace amount of ceria incorporation by atomic layer deposition in Co/CoOx-embedded N-doped carbon for efficient bifunctional oxygen electrocatalysis: demonstration and quasi-operando observations. Int J Hydrogen Energy 2021;46:38258–69. https://doi.org/10.1016/j.ijhydene.2021.09.082.

[32] Kang H-S, Grewal S, Li H, Lee MH. Effect of surface-specific treatment by infiltration into LaNi 6 Fe 4 O 3- δ cathodic backbone for solid oxide fuel cells. J Electrochem Soc 2019;166:F255–63. https://doi.org/10.1149/2.0421904jes.